

Defect detection of solar cells in electroluminescence images using Fourier image reconstruction

Du-Ming Tsai*, Shih-Chieh Wu, Wei-Chen Li

Department of Industrial Engineering & Management, Yuan-Ze University, 135 Yuan-Tung Road, Nei-Li, Tao-Yuan, Taiwan, ROC

ARTICLE INFO

Article history:

Received 22 August 2011

Received in revised form

2 December 2011

Accepted 16 December 2011

Available online 9 January 2012

Keywords:

Defect detection

Surface inspection

Solar cell

Fourier transform

ABSTRACT

Solar power is an attractive alternative source of electricity. Solar cells, which form the basis of a solar power system, are mainly based on crystalline silicon. Many defects cannot be visually observed with the conventional CCD imaging system. This paper presents defect inspection of multicrystalline solar cells in electroluminescence (EL) images. A solar cell charged with electrical current emits infrared light, whose intensity is lower at intrinsic crystal grain boundaries and extrinsic defects of small cracks, breaks, and finger interruptions. The EL image can distinctly highlight barely visible defects as dark objects, but it also shows random dark regions in the background, which makes automatic inspection in EL images very difficult.

A self-reference scheme based on the Fourier image reconstruction technique is proposed for defect detection of solar cells with EL images. The target defects appear as line- or bar-shaped objects in the EL image. The Fourier image reconstruction process is applied to remove the possible defects by setting the frequency components associated with the line- and bar-shaped defects to zero and then back-transforming the spectral image into a spatial image. The defect region can then be easily identified by evaluating the gray-level differences between the original image and its reconstructed image. The reference image is generated from the inspection image itself and, thus, can accommodate random inhomogeneous backgrounds. Experimental results on a set of various solar cells have shown that the proposed method performs effectively for detecting small cracks, breaks, and finger interruptions. The computation time of the proposed method is also fast, making it suitable for practical implementation. It takes only 0.29 s to inspect a whole solar cell image with a size of 550×550 pixels.

© 2011 Elsevier B.V. All rights reserved.

1. Introduction

In recent years, the demand for solar cells has increased significantly due to growing environmental concerns and the global oil shortage. The demand could even be potentially boosted after the nuclear crisis in Fukushima, Japan. Solar cells, which convert the photons from the sun to electricity, are largely based on crystalline silicon in the currently-installed solar power systems because of the competitive conversion efficiency and usable lifespan. Multicrystalline solar cells are more common than monocrystalline solar cells due to lower material and manufacturing costs.

Since defects in solar cells critically reduce their conversion efficiency and usable lifetime, the inspection of solar cells is very important in the manufacturing process. A solar wafer is a thin slice of a cubic silicon ingot. It is further processed and fabricated into a solar cell, which forms the basic unit of a solar power

system. The surface of a multicrystalline solar cell shows multiple crystal grains of random shapes and sizes in random positions and orientations. Fig. 1(a) shows the surface image of a multicrystalline solar wafer. Fig. 1(b) further demonstrates the CCD-captured image of a multicrystalline solar cell, where the vertical thin metal strips are finger electrodes that supply current to the two horizontal bus bars. Crystal grains of random shapes and sizes are displayed on the surface.

Some obvious defects, such as large breaks, can be directly observed from the imaged surface of a solar cell, although the random crystal grain background can camouflage the defects. Some fatal defects, such as small cracks lying within the wafer surface and subtle finger interruptions, may not be visually observed in the image captured by a typical CCD camera.

In order to highlight the intrinsic and extrinsic deficiencies that degrade the conversion efficiency of a solar cell, the electroluminescence (EL) imaging technique [1,2] has been proposed in recent years. In the EL imaging system, the solar cell is excited with voltage, and then a cooled Si-CCD camera or a more advanced InGaAs camera is used to capture the infrared light emitting from the excited solar cell. Areas of silicon with higher conversion efficiency

* Corresponding author. Fax: +03 463 8907.

E-mail address: iedmtsai@saturn.yzu.edu.tw (D.-M. Tsai).

present brighter luminescence in the sensed image. Process deficiencies such as small cracks, breaks, and finger interruptions appear as dark regions in the EL image. Fig. 2 shows the configuration of the EL imaging system. Fig. 3(a) shows the EL image of a defect-free solar cell. Figs. 3(b)–(d) presents three EL images of defective solar cells that contain small cracks, breaks, and finger interruptions, respectively. The defect areas are inactive, resulting in dark regions that are visually observable in the sensed EL image.

By observing both Figs. 3(a) and (b), the EL imaging system not only shows the extrinsic defects as dark objects but also presents the dislocation and grain boundaries with dark gray levels in the sensed image. The background shows inhomogeneous patterns of dark blobs and clouds due to the random crystal grains in the multicrystalline silicon wafer. This characteristic makes the automatic defect detection in EL images very difficult. In this paper, we propose a Fourier image reconstruction scheme to detect small cracks, breaks, and finger interruptions of multicrystalline solar cells in EL images. The proposed Fourier-transform-based scheme can well identify the local defect as long as it is darker than its surroundings in the EL image. The defect contrast is not required to be larger than the grain boundary contrast.

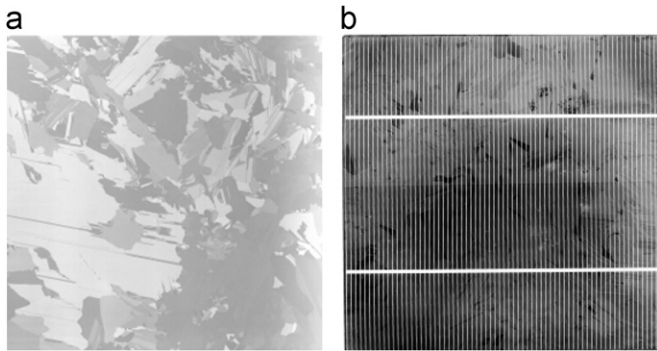


Fig. 1. CCD-captured images of (a) multicrystalline solar wafer and (b) multicrystalline solar cell.

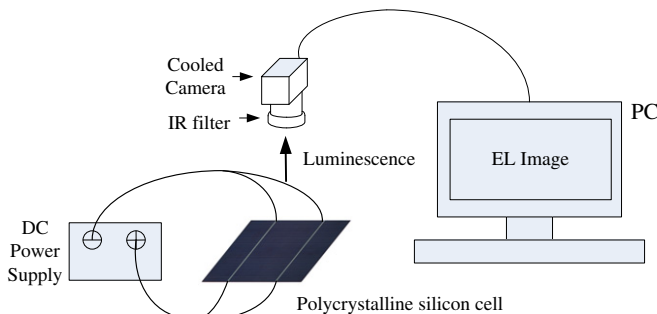


Fig. 2. Configuration of an EL imaging system.

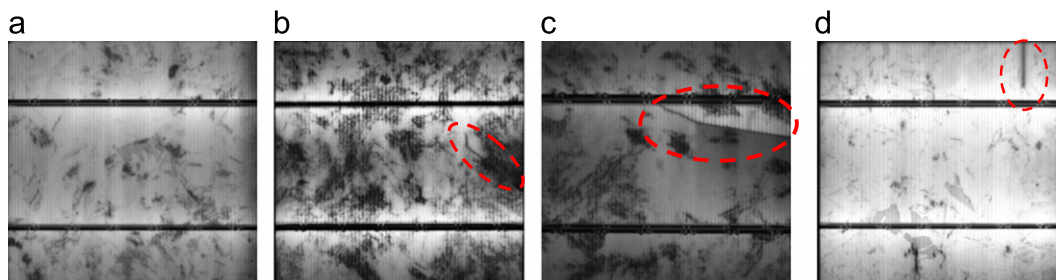


Fig. 3. Demonstrative EL images of solar cells: (a) defect-free sample; (b) small crack; (c) break; (d) finger-interruption.

Texture analysis techniques [3] in image processing have been used for automatic visual inspection of various material surfaces. These defect detection methods mainly aim at homogeneously textured surfaces, in which textural patterns appear repetitively or periodically in the whole image. A set of textural features are generally extracted either from the spatial domain or from the spectral domain of an inspection image, and then a high-dimensional classifier is used for identifying local defects that break the homogeneity of the textured background.

In spatial domain approaches, the widely-used textural features are the second-order statistics derived from spatial gray level co-occurrence matrices [4]. They have been used for the inspection of machined surfaces [5], web surfaces [6], textile fabrics [7], and cotton contamination [8].

In spectral domain approaches, textural features are commonly extracted from the power spectrum of an image by the Fourier transform [9]. They have been used for the inspection of textile fabrics [10,11] and semiconductor wafers [12]. Gabor filter banks with varying frequencies and phase angles are also commonly used to represent texture characteristics, and are applied to the inspection of granite [13], steels [14], and textile fabrics [15,16]. The wavelet transform [17,18] is a powerful tool of multiresolution analysis for textural feature extraction. The discriminant features are generally represented by wavelet energies of decomposed subimages in different frequency channels and scales. They have been applied to the inspection of semiconductor wafers [19] and textile fabrics [20,21].

The local feature extraction techniques above work successfully only for defect detection in uniform and homogeneously-textured surfaces. They cannot be extended to defect detection in heterogeneously-textured surfaces, such as EL images of multicrystalline solar cells. For solar wafer and solar cell inspection, Fu et al. [22] presented a machine vision method to detect cracks in solar cells. The method can identify only cracks in the cell edges having gray levels distinct from their surroundings. Ordaz and Lush [23] analyzed the conversion efficiency of a solar cell based on the gray-level distribution in the EL image. Pilla et al. [24] used the thermographic technique to highlight cracks in solar cells. Demant et al. [25] studied the quality of multicrystalline solar wafers using the photoluminescence imaging (PL) technique. The quality features are combined in a histogram for an interpretable presentation, and are used to establish a rating of wafer quality. Haunschild et al. [26] analyzed crystallization-related features of solar wafers in PL images. It is shown that the fraction of crystal defects, defined as the pixels covered by crystal defects divided by the total number of pixels of the wafer, is highly correlated with the open circuit voltage. Warta [27] reviewed various sensing techniques for defect and impurity diagnostics in silicon solar cells.

Recently, Tsai et al. [28] presented an anisotropic diffusion algorithm for detecting small cracks that are visible on the solar wafer surface. The sensed image, obtained from a typical CCD camera and light source, shows micro-cracks with low gray levels

and high gradients. The diffusion process smoothes the suspected defect region and preserves the crystal grain background. The crack location can then be well detected by subtracting the diffused image from the original image. Tsai and Luo [29] further proposed a mean-shift algorithm to detect three defect types of saw-mark, fingerprints, and contamination in multicrystalline solar wafers. The target defects generally present highly variable gradient directions, while crystal grain edges show more consistent gradient directions. The original gray-level wafer image is first converted into an entropy image, where each pixel defined in a small neighborhood window is represented by the entropy of gradient directions. The mean-shift smoothing process is then performed to remove noise and grain edges in the entropy image. The final edge points remaining in the filtered image are identified as defective ones. Chiou and Liu [30] used a near infrared imaging system to detect micro-cracks in solar wafers. In the resulting images, the intensities of a micro-crack are darker than those of the surrounding grain background. Local thresholding and region-growing segmentation, followed by morphological post-processing and blob analysis, are used to detect dark micro-cracks. The method is performed on the solar wafer level and assumes that the sensed micro-crack is significantly darker than the crystal grains under infrared lighting. However, with that method, a dark, thin, elongated crystal grain in the defect-free solar wafer could be falsely identified as a defect. Li and Tsai [31] presented a machine vision algorithm to detect saw-mark defects in multicrystalline solar wafers in the wafer cutting process. The Fourier transform is used to smooth the crystal grain background as a non-textured surface. A line detection process is then carried out for each individual scan line of the filtered image to detect possible defect points that are distinctly apart from the line sought.

In this study, we further the development of an automatic detection method for critical surface defects of both exterior and interior small cracks, breaks, and finger interruptions of a multicrystalline solar cell in an electroluminescence image. The small crack appears as a thin line segment, and the break divides the infected area into a dark and a bright region in the EL image. The boundary of the break is also line-shaped. The disconnected finger affects the area beneath the finger and its neighborhood and appears as a dark bar-shaped object along the finger direction in the EL image. As seen in Figs. 3(b)–(d), all three types of defects are line- or bar-shaped. In order to detect such defects against an inhomogeneous background, a self-reference scheme based on the Fourier image reconstruction is proposed for solar cell inspection in EL images.

The Fourier spectrum is noise-insensitive and is ideally suited for representing the directionality of lines in a complicated spatial image. In the Fourier spectrum of an EL image, the high-energy frequency components corresponding to the random background are spread circularly around the DC center in the spectrum image. The directional line of a crack/break or the elongated bar of a finger interruption in the EL image clearly corresponds to high-energy frequency components, which are spread along the line in the Fourier spectrum image with a direction orthogonal to its counterpart in the spatial image. The frequency components lying in the vicinity of the line in the spectrum image are eliminated by setting them to zero. The revised spectrum image is then back-transformed by using the inverse Fourier transform (IFT). The IFT process will remove the line- and bar-shaped defects and preserve the original background pattern in the reconstructed image. The filtered image can be treated as a defect-free image. It is then used as a self-reference image for comparison. By subtracting the gray values between the reconstructed image and the original EL image pixel by pixel, a defect point will yield a distinctly large gray-level difference. A simple statistical control limit can be finally applied to set the threshold of gray-level differences for

segmenting the defect region from the background in the difference image. To detect a line associated with a line-shaped defect in an arbitrary orientation in the spectrum image, a fast Hough transform along with a verification check is also developed to identify all the angles of defect lines.

This paper is organized as follows: Section 2 first discusses the Fourier transform and the properties of line- and bar-shaped defects in the spectrum image. The Hough transform and the verification process used to detect slope angles associated with line- and bar-shaped defects in the spectrum image are next presented. An image reconstruction process using the inverse Fourier transform, followed by image difference and automatic thresholding, is then discussed in detail. Section 3 presents the experimental results on a large number of multicrystalline solar cells containing a variety of defects. The effect of changes in parameter values on the detection results is also evaluated. The paper is concluded in Section 4.

2. Defect detection in inhomogeneous surfaces

Self-reference approaches [32,33] that generate a golden template from the inspection image itself and image reconstruction approaches [34,35] that remove the background pattern have been used for defect detection in textured surfaces. They are based on the assumption that the self-similar texture is periodically present everywhere in the surface or that a complex pattern repetitively appears in the image. These approaches can only be applied to surfaces with homogeneous textures or repetitive patterns. The multicrystalline solar cell in the EL image falls in the category of inhomogeneous textures. Conventional self-reference or image reconstruction methods cannot be directly extended for defect detection in randomly-textured surfaces.

The Fourier transform is a powerful tool to describe periodical signals. Since the crystal grain background in the EL image does not show periodical and repetitive patterns, the frequency components corresponding to the grain background cannot be identified in the spectrum image. As shown in Figs. 3(b)–(d), the defects found in the EL image present as line- or bar-shaped objects. It is well known that a line segment in the spatial domain image will also spread along the line orthogonal to its original orientation, passing through the DC center in the Fourier spectrum image. Therefore, any lines found in the spectrum image could potentially indicate a defect in the solar cell. The Fourier transform is a global representation of an image and, thus, gives no spatial information of the defect in the original EL image. In order to locate a defect in the EL image, we can eliminate the frequency components along a line with a specific slope angle in the spectrum image and then back-transform the image using the inverse Fourier transform. The reconstructed image can then be used as a defect-free reference image for comparison. Each individual EL image for inspection can rebuild its own reference image. By subtracting the original EL image from its reconstructed reference image, a pixel with a significant gray-level difference larger than a threshold is declared as a defect point. This self-reference approach with the Fourier image reconstruction can be effectively applied to EL images with random grain backgrounds, and it is not affected by any environmental changes such as lighting.

2.1. Fourier image reconstruction

Let $f(x,y)$ be the gray level at pixel coordinates (x, y) in an EL image of size $M \times N$. The two-dimensional discrete Fourier

transform (DFT) of $f(x,y)$ is given by

$$F(u,v) = \sum_{y=0}^{N-1} \sum_{x=0}^{M-1} f(x,y) \cdot \exp \left[-j2\pi \left(\frac{ux}{M} + \frac{vy}{N} \right) \right] \quad (1)$$

for spectral variables $u=0, 1, 2, \dots, M-1$ and $v=0, 1, 2, \dots, N-1$. The DFT is generally complex; that is,

$$F(u,v) = R(u,v) + j \cdot I(u,v) \quad (2)$$

where $R(u,v)$ and $I(u,v)$ are the real and imaginary parts of $F(x,y)$, i.e.,

$$R(u,v) = \sum_{y=0}^{N-1} \sum_{x=0}^{M-1} f(x,y) \cdot \cos \left[2\pi \left(\frac{ux}{M} + \frac{vy}{N} \right) \right] \quad (3a)$$

$$I(u,v) = \sum_{y=0}^{N-1} \sum_{x=0}^{M-1} f(x,y) \cdot \sin \left[2\pi \left(\frac{ux}{M} + \frac{vy}{N} \right) \right] \quad (3b)$$

The power spectrum $P(x,y)$ of $F(x,y)$ is defined as

$$P(u,v) = |F(u,v)|^2 = R^2(u,v) + I^2(u,v) \quad (4)$$

Since the input image $f(x,y)$ is real, the FT exhibits conjugate symmetry. The magnitude of the transform is symmetric with respect to the DC center in the spectrum image. Fig. 4(a1) is the EL image of a defect-free solar cell of size 550×550 pixels. The corresponding Fourier spectrum in Fig. 4(a2) shows that the high-energy frequency components spread circularly in the spectrum image for the random grain background. The vertical bright line in the spectrum image represents the two horizontal bus bars. The bright spots in the horizontal line in the spectrum image

represent the vertical thin fingers of the solar cell. The distance between the spots in the spectrum image is associated with the spacing of fingers in the spatial image. Fig. 4(b1) shows the EL image of a defective solar cell that contains a small line crack at an angle of 37° , and Fig. 4(b2) is the corresponding Fourier spectrum image. It is expected to find a 127° high-energy straight line passing through the DC center in the spectrum image. However, the resulting spectrum image cannot sufficiently display a visible line due to the extremely short line segment of the small crack with respect to the whole EL image area.

In order to intensify the high-energy line for a defect with either a long or a short line segment in the Fourier spectrum image, the original solar cell image is equally divided into many non-overlapping subimages of smaller size. Fig. 4(c1) shows the crack defect in a 75×75 subimage. Fig. 4(c2) presents the corresponding Fourier spectrum, where the high-energy line associated with the 37° crack is now more distinctly present at 127° in the spectrum image. The Fourier transform of a small EL subimage not only gives a better representation of line- and bar-shaped defects in a random background but also provides a better computational efficiency, as compared to the process results in the whole image of a large size.

The choice of an adequate subimage size is generally related to the defect size present in the EL image. The window size should be selected such that the defect line in its associated spectrum image can sufficiently present a significant local peak of the accumulated power spectrum. As a rule of thumb, a satisfactory detection results can be always achieved if a defect to be inspected in the window is at least half of the window width. A preliminary experiment has indicated that the proposed method generates consistent detection results for varying window sizes between 55×55 and 95×95 pixels.

2.2. Line detection in spectrum images

To automatically detect high-energy lines associated with line-shaped defects in the Fourier spectrum image, we propose a two-stage line detection process for the task. The first stage of the line detection process uses the Hough transform (HT) to find the slope angles of suspected lines in the spectrum image, and the second stage uses a verification rule to remove false angles detected in the first stage.

Step 1: The Hough transform

The Hough transform is an effective technique for line detection under noisy and discontinuous conditions. It involves a voting process that transforms the set of points in the image space into a set of accumulated votes in the parameter space. A local peak larger than some threshold in the parameter space then indicates a line present in the image space. The conventional HT is computationally intensive for real-time, on-line applications due to the large search space of parameter values. Fortunately, the implementation of the HT line detection in the spectrum image is very easy and fast because every line will pass through the DC center of the spectrum image. The line equation is then solely defined by the parameter of slope angle.

The HT process scans every pixel (u,v) in the spectrum image, and calculates the slope angle

$$\theta = \tan^{-1} \left(\frac{v-v_0}{u-u_0} \right) \quad (5)$$

where (u_0, v_0) is the central coordinates of the spectrum image, and is given by $(M/2, N/2)$ for an image of size $M \times N$. The voting weight for the one-dimensional accumulator $A(\theta)$ at slope angle θ is given by the Fourier spectrum $|F(u,v)|$; i.e.,

$$A(\theta) \leftarrow A(\theta) + |F(u,v)|$$

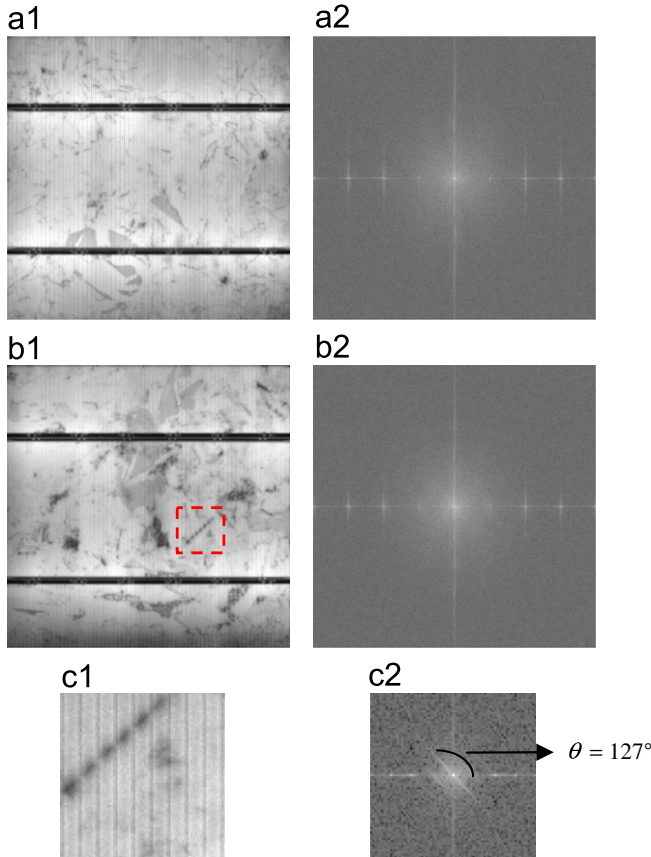


Fig. 4. Fourier spectrum images of solar cells: (a1) defect-free EL image; (a2) spectrum image of (a1); (b1) full-sized defective EL image of 550×550 pixels; (b2) spectrum image of (b1) where no lines can be visually observed; (c1) small crack in a 75×75 EL subimage; (c2) spectrum image of (c1), where a 127° line can be distinctly observed.

A local peak with significantly large accumulated magnitude indicates a possible line in the spectrum image. Due to the inherited structure of a solar cell in the EL image, the accumulator will show extremely high magnitudes in horizontal, vertical, and diagonal directions, i.e., angles at 0° , 45° , 90° and 135° . Figs. 5(a1) and (b1) show a defect-free and a defective EL subimage of solar cells, respectively. Figs. 5(a2) and (b2) are the corresponding accumulators $A(\theta)$ for the EL subimages in Figs. 5(a1) and (a2), excluding the accumulated values at 0° , 45° , 90° and 135° . It can be seen that there are no significant peaks for the Fourier spectrum of the defect-free subimage. However, there is a distinct peak at $\theta=127^\circ$ corresponding to the 37° crack in the EL subimage.

Since individual solar cells have different random backgrounds in the EL images, no fixed threshold can be predetermined to identify the slope angles of all suspected lines in different spectrum images. The threshold used to pick up the slope angles of lines in each individual spectrum image must be adaptively determined. In this study, the adaptive threshold for θ selection is given by the upper bound of a simple statistical control limit, which is defined as the mean deviated from a multiple constant of standard deviation of a random variable. The angle threshold T_θ is thus given by

$$T_\theta = \mu_{A(\theta)} + K_\theta \cdot \sigma_{A(\theta)} \quad (6)$$

where $\mu_{A(\theta)} = 1/176 \sum_{\theta} A(\theta)$, $\theta \neq 0^\circ, 45^\circ, 90^\circ$ and 135°

$$\sigma_{A(\theta)} = \left\{ \frac{1}{175} \sum_{\theta} [A(\theta) - \mu_{A(\theta)}]^2 \right\}^{1/2}$$

K_θ = user specified control constant; it is given by 2.5 in this study.

Note that we exclude 0° , 45° , 90° and 135° for the computation of the mean $\mu_{A(\theta)}$ and standard deviation $\sigma_{A(\theta)}$ of $A(\theta)$. All local maximum peaks with $A(\theta)$ greater than the angle threshold T_θ are recognized as suspected slope angles of defects, and are collected in a set:

$$\Theta_1 = \{\theta | A(\theta) > \mu_{A(\theta)} + K_\theta \cdot \sigma_{A(\theta)}\} \quad (7)$$

Because defects may also be present in the directions of 0° , 45° , 90° and 135° , they are included in the collection Θ_1 of the 1st stage of line detection.

The parameter K_θ in Eq. (6) is used to select potential defect lines in the image. A tight threshold (i.e. a small K_θ value) can be used to identify all suspected defect lines. All the selected line angles can then be reliably verified in step 2 (Eq. (11) below) that does not need any parameter values. Since a true line crack generally results in distinctly high-energy frequency components in the spectrum image, setting $K_\theta=2.5$ in this study is sufficiently small to ensure all true crack lines in the associated spectrum image can be selected.

Step 2: Line angle verification

The suspected line angles detected by the Hough transform in the first stage may contain false lines due to the random grain background in the EL image. We need further identify the false line angles and remove them from the collection Θ_1 . Let $L_{\theta^*, 0}$ represent a line with slope angle θ^* , for $\theta^* \in \Theta_1$, passing through the center (u_0, v_0) in the spectrum image. The line equation of $L_{\theta^*, 0}$ is given by

$$L_{\theta^*, 0} : (u - u_0) \cdot \tan \theta^* - (v - v_0) = 0 \quad (8)$$

Denote by $L_{\theta^*, \Delta s}$ the line parallel to $L_{\theta^*, 0}$ with a shift of Δs , where Δs is defined as the perpendicular distance from $L_{\theta^*, \Delta s}$ to the center (u_0, v_0) . Therefore, the line equation of $L_{\theta^*, \Delta s}$ is given by

$$L_{\theta^*, \Delta s} : (u - u_0) \cdot \tan \theta^* - (v - v_0) + \frac{\Delta s}{2 \cos \theta^*} = 0 \quad (9)$$

Fig. 6 sketches the lines $L_{\theta^*, \Delta s}$ with $-S \leq \Delta s \leq S$ for some shift range $\pm S$. In this study, the range S is set at 10. We then project the Fourier spectrum $|F(u, v)|$ of each line $L_{\theta^*, \Delta s}$ by accumulating the Fourier spectra for all frequency components along the line; i.e.,

$$H_{\Delta s}(\theta^*) = \sum_{(u, v) \in L_{\theta^*, \Delta s}} |F(u, v)| \quad (10)$$

For a true defect line in the spectrum image, the spread of frequency components will concentrate along the line $L_{\theta^*, 0}$ and gradually decrease when they are apart from the line. Conversely, a false defect line may not show the projection peak at $L_{\theta^*, 0}$. Instead, the projection in the vicinity of $L_{\theta^*, 0}$ could give a larger projection magnitude, or it does not show a monotonic decrease of projection magnitude when it is away from $L_{\theta^*, 0}$. Figs. 7(a) and (b) shows the EL subimage of a small crack and its corresponding spectrum image, where the crack appears as a 63° line in the spectral space. Figs. 7(c)–(f) presents the profiles of the projection

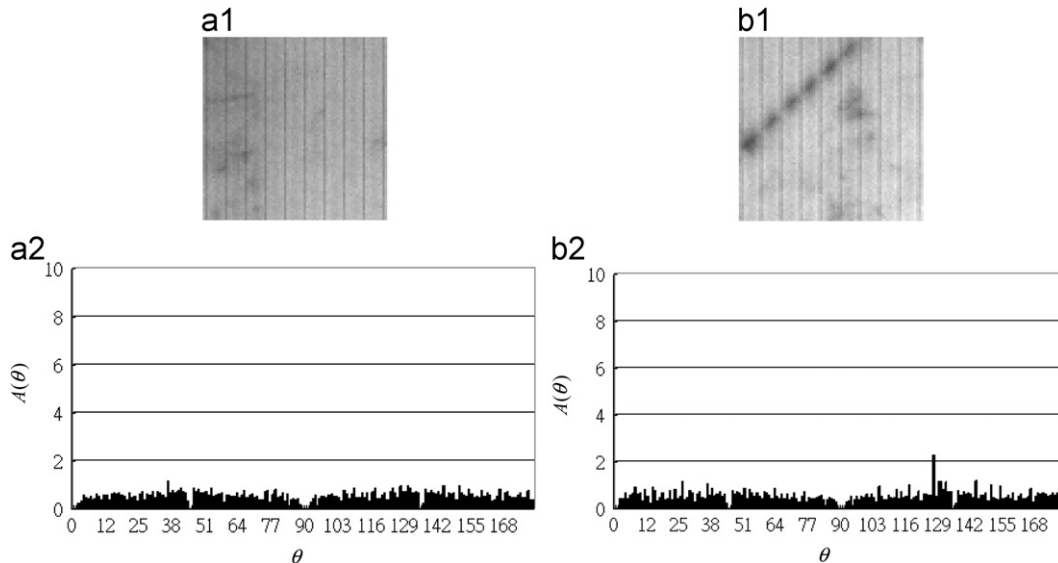


Fig. 5. The accumulator $A(\theta)$ of the Hough transform: (a1) defect-free EL subimage; (b1) defective EL image with a 37° -crack; (a2) accumulator $A(\theta)$ as a function of θ for defect-free sample (a1); (b2) accumulator $A(\theta)$ for defective sample (b1).

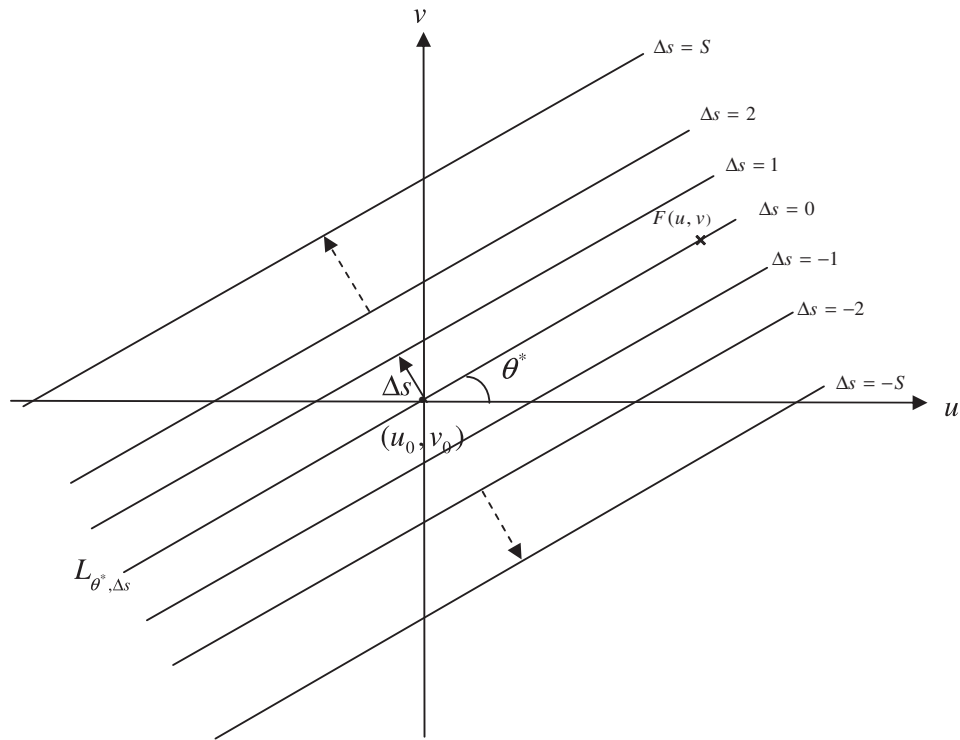


Fig. 6. Sketch of lines parallel to $L_{\theta^*,0}$ with a shift of Δs .

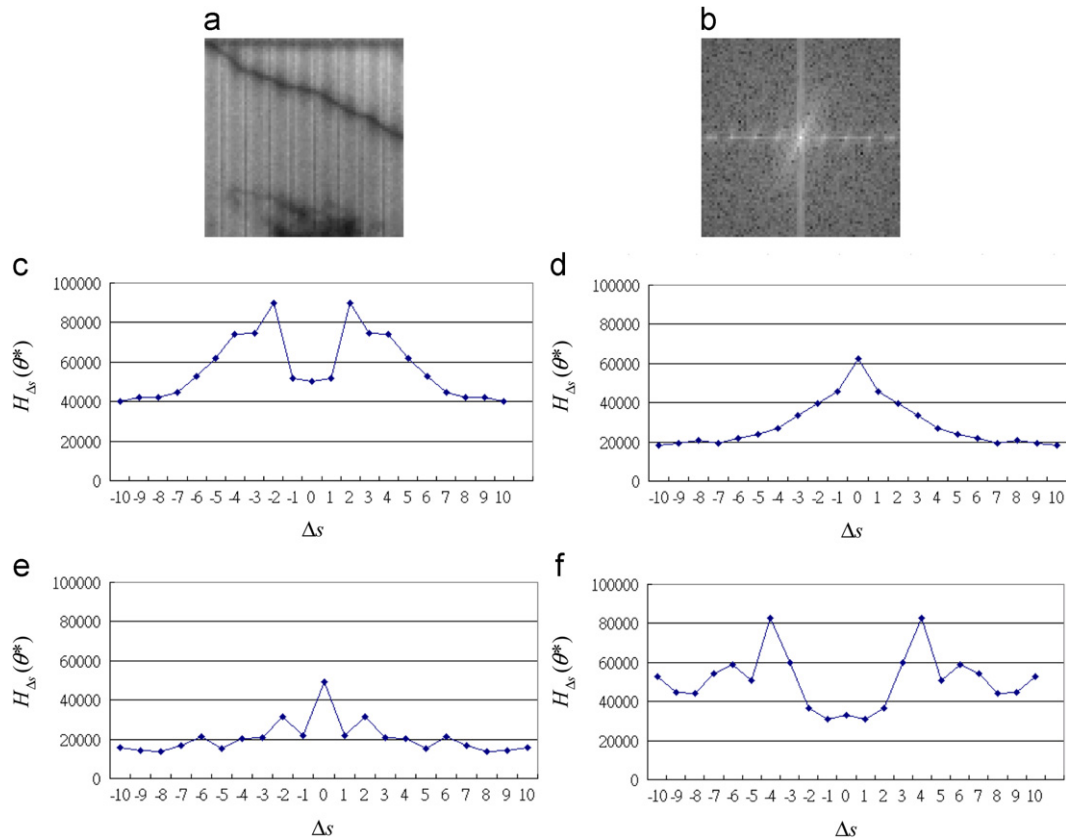


Fig. 7. Profiles of projection $H_{\Delta s}(\theta^*)$: (a) EL subimage of a small crack; (b) Fourier spectrum image showing a high-energy line at 63° ; (c)–(f) profiles of the line projection at angles 45° , 63° , 68° and 135° , respectively.

magnitudes $H_{\Delta s}(\theta^*)$ as a function of the shift Δs for slope angles 45° , 63° , 68° and 135° . Each profile $H_{\Delta s}(\theta^*)$ is symmetric with respect to $\Delta s = 0$. The high-energy projections at 45° and 135° do

not show the maximum peak at $\Delta s = 0$, and $H_{\Delta s}(68^\circ)$ near the true line angle of 63° does not show a monotonic decreasing profile. This phenomenon also holds for the break defect. Therefore, the

slope angles retained for further consideration are those showing a monotonic decrease of $H_{\Delta s}(\theta^*)$. The final collection of slope angles after the angle verification in the 2nd stage is given by

$$\Theta_2 = \{\theta^* | \theta^* \in \Theta_1 \text{ and } H_{\Delta s}(\theta^*) > H_{\Delta s+1}(\theta^*)\} \quad (11)$$

2.3. Defect removal

To tackle the problem of defect detection in an inhomogeneous surface, we remove all the possible defects and create a near defect-free reference image from each individual test image under inspection. This is done by assigning zero values to all frequency components in the vicinity of each detected line with slope angle θ^* in the collection Θ_2 , and then back-transforming the revised Fourier spectrum using the inverse discrete Fourier transform.

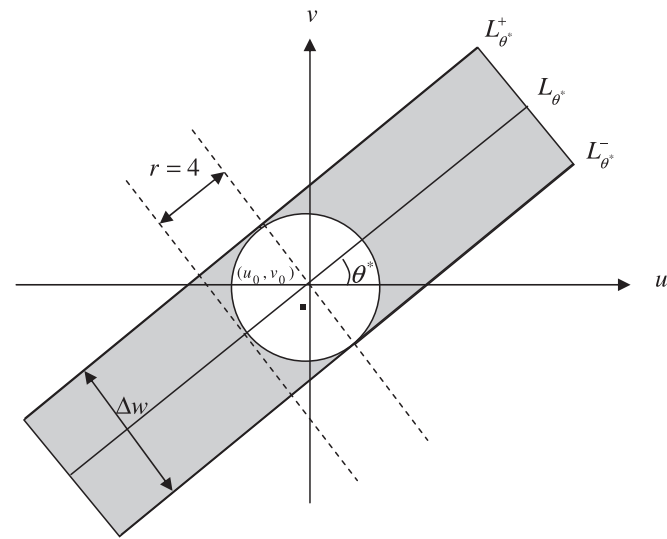


Fig. 8. Band-rejection region in the Fourier spectrum image for defect removal.

Let Δw be the band-rejection width. It is given as 5 in this study for defect removal. For a given slope angle θ^* , $\theta^* \in \Theta_2$, the band-rejection region is bounded by two lines $L_{\theta^*}^+$ and $L_{\theta^*}^-$ that are parallel to $L_{\theta^*}^0$ with a width of Δw between these two lines, as shown in Fig. 8. The bounded lines $L_{\theta^*}^+$ and $L_{\theta^*}^-$ are given by

$$L_{\theta^*}^+ : (u-u_0)\tan\theta^* - (v-v_0) + b = 0 \quad (12a)$$

$$L_{\theta^*}^- : (u-u_0)\tan\theta^* - (v-v_0) - b = 0 \quad (12b)$$

where $b = |\Delta w/2/\cos\theta^*|$

For any pixel (u, v) in the Fourier spectrum image that lies within the band-rejection region, i.e.

$$L_{\theta^*}^+ \geq 0 \text{ and } L_{\theta^*}^- \leq 0,$$

the associated $F(u, v)$ is set to zero.

As discussed previously, the approximation of the global background pattern of an EL image is represented by the low-frequency components around the DC center in the spectrum image. To preserve the background pattern in the reconstructed image, all frequency components lying within a small circle with the DC as the center must be retained without changing their spectrum values. Based on the removal process discussed above, the revised Fourier spectrum is given by

$$\hat{F}(u, v) = \begin{cases} 0, & \text{if } L_{\theta^*}^+ \geq 0 \text{ and } L_{\theta^*}^- \leq 0 \text{ \& } (u-u_0)^2 + (v-v_0)^2 > r^2 \\ F(u, v), & \text{otherwise} \end{cases}$$

In this study, the circular radius r is set to 4 for a 75×75 EL subimage. The self-reference image of an inspection image $f(u, v)$ of size $M \times N$ can now be reconstructed by the inverse discrete Fourier transform. Hence,

$$\hat{f}(x, y) = \frac{1}{M \cdot N} \sum_{v=0}^{N-1} \sum_{u=0}^{M-1} \hat{F}(u, v) \cdot \exp\left[j2\pi\left(\frac{ux}{M} + \frac{vy}{N}\right)\right] \quad (13)$$

Note that the defect-free reference image $\hat{f}(x, y)$ is created from the inspection image $f(u, v)$ itself. Defects in the EL subimage can be easily identified by subtracting the original image $f(u, v)$ from the reconstructed image $\hat{f}(x, y)$. The image difference

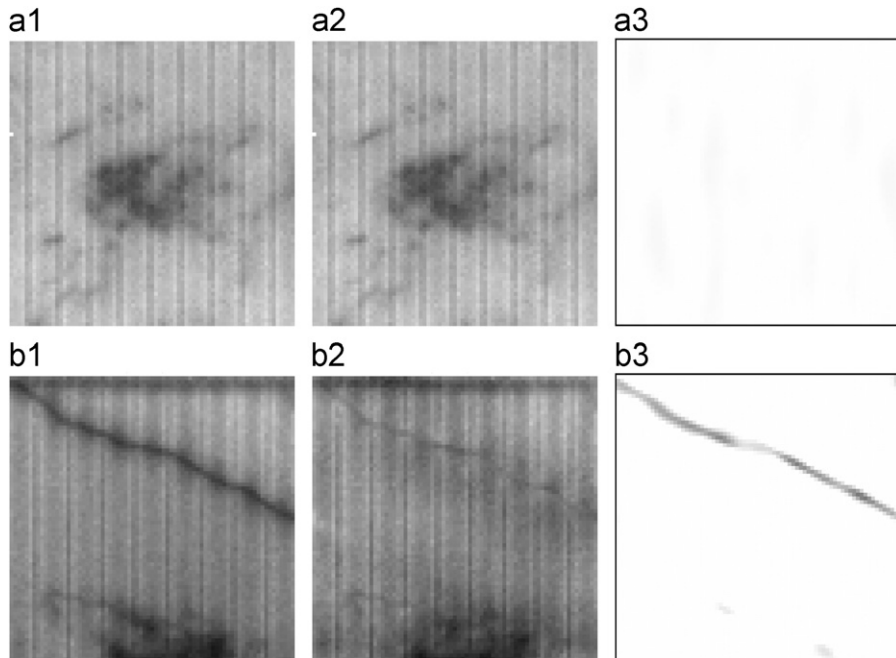


Fig. 9. Image reconstruction and image difference: (a1) defect-free EL subimage; (b1) defective EL subimage; (a2), (b2) respective reconstructed images; (a3), (b3) respective difference images.

between $f(u, v)$ and $\hat{f}(x, y)$ is given by

$$\Delta f(x, y) = |f(x, y) - \hat{f}(x, y)| \quad (14)$$

A small difference value of $\Delta f(x, y)$ indicates a defect-free point at (u, v) , whereas a distinctly large difference shows strong evidence of a defect point. The upper bound of a simple statistical control limit is thus used to set the threshold for segmenting defects from the background in the difference image $\Delta f(x, y)$. The threshold for $\Delta f(x, y)$ is given by

$$T_{\Delta f} = \mu_{\Delta f} + K_{\Delta f} \cdot \sigma_{\Delta f} \quad (15)$$

where $\mu_{\Delta f}$ and $\sigma_{\Delta f}$ are the mean and standard deviations of $\Delta f(x, y)$ in the whole image, and $K_{\Delta f}$ is a pre-determined control constant. The detection results can be represented by a binary image, wherein the pixel (x, y) with $\Delta f(x, y) > T_{\Delta f}$ is a defect point and is marked in black. It is otherwise a defect-free point and is marked in white in the binary image. Figs. 9(a1) and (b1) show, respectively, a defect-free and a small crack subimage. Their reconstructed images are presented in Figs. 9(a2) and (b2). Figs. 9(a3) and (b3) are the corresponding difference images $\Delta f(x, y)$. The results show that the reconstructed image of the defect-free sample is similar to its original one, and no significant differences are found in the difference image. In contrast, the reconstructed image of the defective sample effectively blurs the small crack, and the difference magnitudes of the defect region are dramatically large in the resulting image. Notice that the defective image in Fig. 9(b1) contains a crack with a mean gray value of 74 and grain boundaries with a mean gray value of 55. The crack contrast is lower than the grain boundary contrast. The proposed Fourier image reconstruction method can still well detect the crack.

2.4. Removal of finger interruption

In the image reconstruction process, special care must be given to finger interruptions. Since the solar cell presents periodical thin finger lines in the vertical direction and the bar-shaped finger interruption also appears vertically in the EL image, removal of all frequency components along the horizontal direction (i.e. $\theta = 0^\circ$) in the Fourier spectrum image will remove all finger lines in the reconstructed image. The subsequent image subtraction between the inspection image and the reconstructed image will then inevitably identify the normal finger lines as defects. To cope with such a problem, only a short horizontal band-rejection region is used to remove the possible bar-shaped defects of finger interruption in the low-frequency region and retain the high-frequency components for the periodical finger lines in the spectrum image.

Fig. 10(a) shows the EL image of a finger interruption, where the repetitive thin vertical lines are the normal fingers. Fig. 10(b) is the corresponding spectrum image. Fig. 10(c1) displays the revised spectrum image, where the horizontal black strip across over the entire image represents the band-rejection region. Figs. 10(c2) and (c3) are, respectively, the difference image and the resulting binary image with $K_{\Delta f} = 1$. It shows that the normal finger lines in the difference image are falsely detected as defects in the binary image. By using a short horizontal band-rejection strip with length of 10 pixels and width of 5 pixels in a 75×75 EL subimage, the bar-shaped defect can be reliably identified without segmenting the normal finger lines as defects, as seen in Figs. 10(d1)–(d3). The specific band-rejection strip in slope angle 0° is applied for every inspection image.

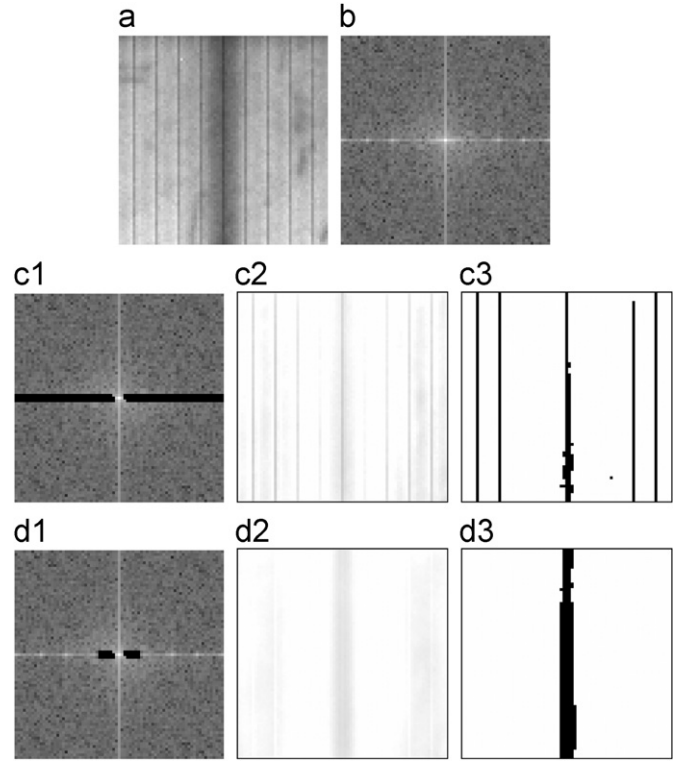


Fig. 10. Removal of vertical finger interruption in the reconstructed image: (a) EL subimage of a finger interruption; (b) Fourier spectrum image; (c1)–(c3) revised spectrum image with band-rejection length $L = 75$, difference image, and binary image, respectively; (d1)–(d3) revised spectrum image with band-rejection length $L = 10$, difference image, and binary image, respectively.

3. Experimental results

In this section, we present the experimental results from a set of multicrystalline solar cells that contain defect-free samples of random backgrounds and defective samples of various defect types in EL images. All experiments were implemented on a personal computer with a Pentium Core 2 Duo 3.00 GHz processor. The whole image of a solar cell is 550×550 pixels wide with 8-bit gray levels. Each solar cell image is divided into small non-overlapping subimages of size 75×75 pixels. The computation time for a 75×75 subimage is only 0.006 s. The proposed method achieves a fast processing time of 0.29 s for on-line inspection of a whole solar cell with a size of 550×550 pixels.

In the proposed algorithms, two critical parameters, the width Δw of the band-rejection region for image reconstruction and the control constant $K_{\Delta f}$ for thresholding the difference image, may affect the detection results. The effects of changes in the parameter values of Δw and $K_{\Delta f}$ are individually evaluated in the following two subsections.

3.1. Effect of band-rejection width Δw

The band-rejection width Δw determines the region for removing the frequency components that correspond to line- and bar-shaped defects. Too small a width may not effectively remove the possible defects in the reconstructed image, and as a result, the true defects will not appear in the difference image. It then may cause mis-detection of defects in the resulting binary image. However, too large a width removes the frequency components not only of the defects but also of the dark regions in the background. The difference image between the original EL image and its reconstructed image will distinctly present the

defect regions at the expense of severe noise on the background. It may then generate false alarms for defect-free solar cells.

Figs. 11(a) and (b) show a crack image and its corresponding Fourier spectrum, respectively. Figs. 11(c1)–(e1) presents the band-rejection region at $\theta = 63^\circ$ with varying widths of $\Delta w = 1, 5$, and 9. Figs. 11(c2)–(e2) are the corresponding reconstructed images, Figs. 11(c3)–(e3) are the difference images, and Figs. 11(c4)–(e4) are the resulting binary images with control constant $K_{\Delta f} = 1$. It can be seen in Figs. 11(c1)–(c4) that a very small width of $\Delta w = 1$ does not present the small crack in the difference image. A large width of $\Delta w = 9$ generates a minor noisy region in the difference image, as shown in Figs. 11(e1)–(e4). Extensive experiments on a large number of EL images with various defect samples have shown that a band-rejection width of 3, 5, or 7 has similar detection performance for a subimage of size 75×75 . The moderate width of $\Delta w = 5$ is therefore used for all test samples in the subsequent experiments.

As noted in Fig. 11(a), a small portion of grain boundaries that has similar orientation as the crack is also presented in the segmented image. This exceptional observation is discussed as

follows. Generally, the random grain boundaries present only short, blurred line segments in the EL image. In the case that the grain boundaries have the same orientation as the defect, the solar cell image under inspection can be still correctly identified as a defective one with extra line segments in the resulting binary image. The detected short fragment can be easily removed by a postprocessing such as morphological operations or blob analysis in the binary image.

3.2. Effect of control constant $K_{\Delta f}$

The statistical control limit $\mu_{\Delta f} + K_{\Delta f} \cdot \sigma_{\Delta f}$ is used to set the threshold for segmenting defect pixels from the background in the difference image $\Delta f(x, y)$. The control constant represents a $K_{\Delta f}$ -multiplication of the standard deviation. Too small a control value of $K_{\Delta f}$ gives a tight threshold and may result in false alarms due to identification of the background points as defect points. However, too large a control value gives a loose threshold and may mis-detect some true defect points.

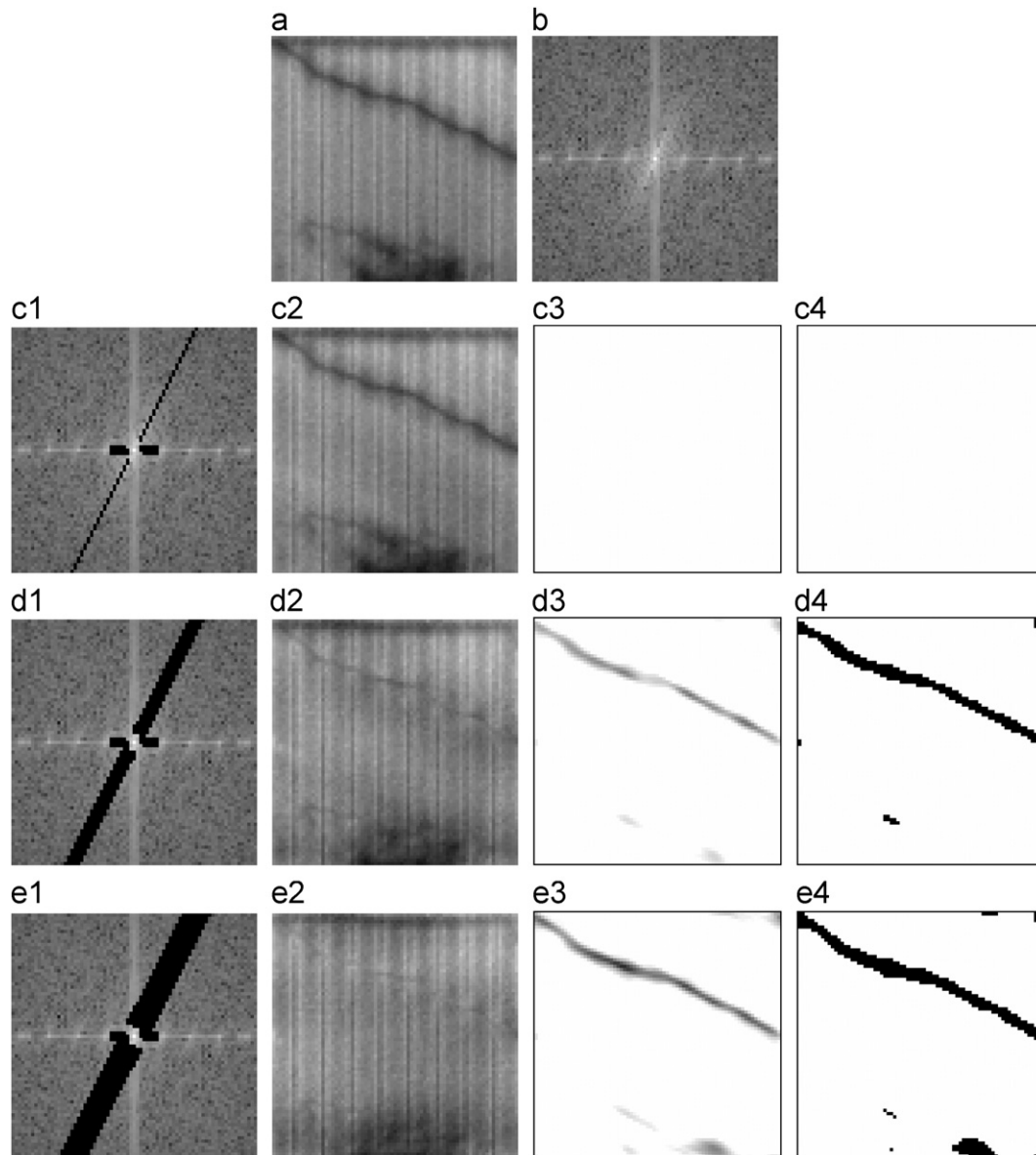


Fig. 11. Effect of changes in band-rejection width Δw : (a) crack subimage; (b) Fourier spectrum image; (c1)–(e1) band-rejection widths of 1, 5 and 9, respectively; (c2)–(e2) respective reconstructed images; (c3)–(e3) respective difference images; (c4)–(e4) respective binary images with $K_{\Delta f} = 1$.

Figs. 12(a1)–(c1) show a set of three defect-free images for the test. Figs. 12(a2)–(c2) are the corresponding reconstructed images, and Figs. 12(a3)–(c3) are the difference images. Figs. 12(a4)–(c4), (a5)–(c5), and (a6)–(c6) are the segmentation results of the difference images with control constants $K_{\Delta f} = 1, 1.5$, and 2, respectively.

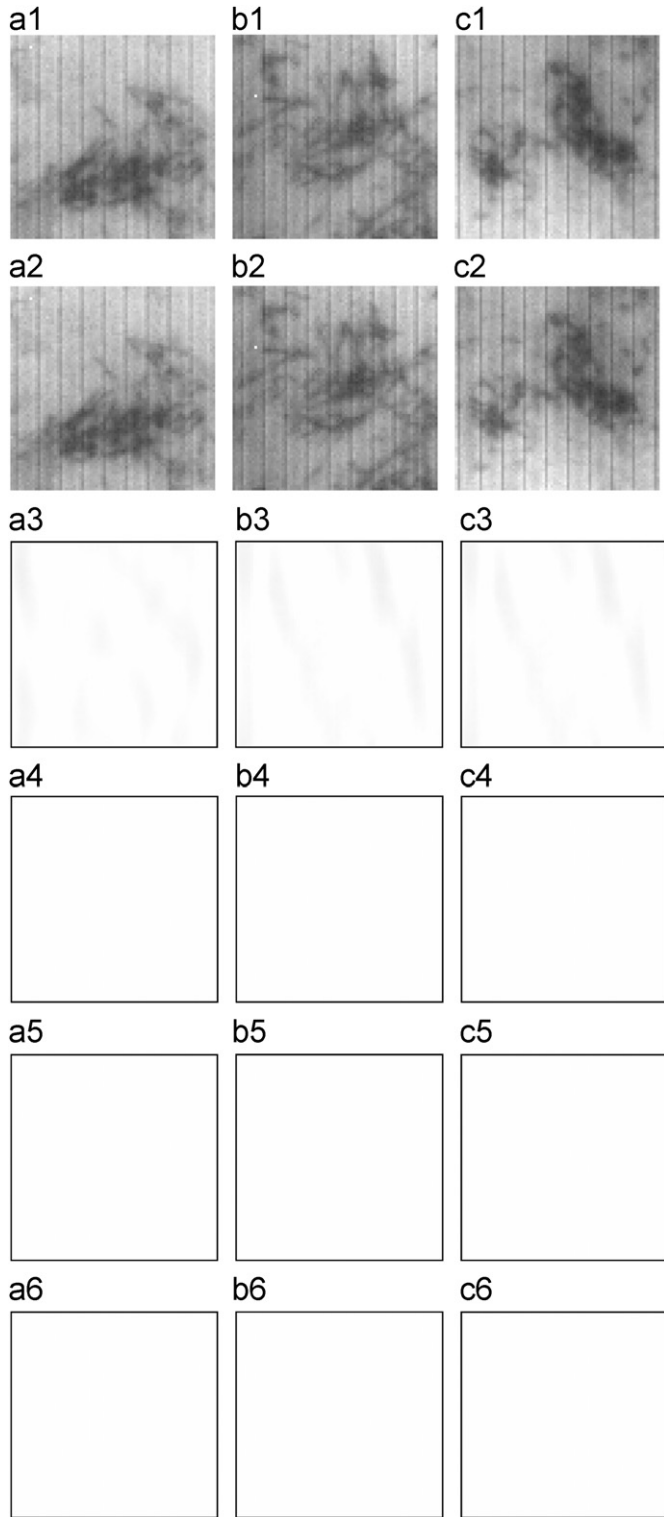


Fig. 12. Effect of changes in control constant $K_{\Delta f}$ for defect-free solar cells: (a1)–(c1) defect-free EL subimages; (a2)–(c2) respective reconstructed images; (a3)–(c3) respective difference images; (a4)–(c4) segmentation results with $K_{\Delta f} = 1$; (a5)–(c5) segmentation results with $K_{\Delta f} = 1.5$; (a6)–(c6) segmentation results with $K_{\Delta f} = 2$.

Figs. 13(a1)–(c1) further present a set of three defective EL images of small crack, break and finger interruption, respectively. Figs. 13(a2)–(c2) and (a3)–(c3) are the reconstructed images and the resulting difference images. Figs. 13(a4)–(c4), (a5)–(c5), and (a6)–(c6) show the detection results as binary images with control constants

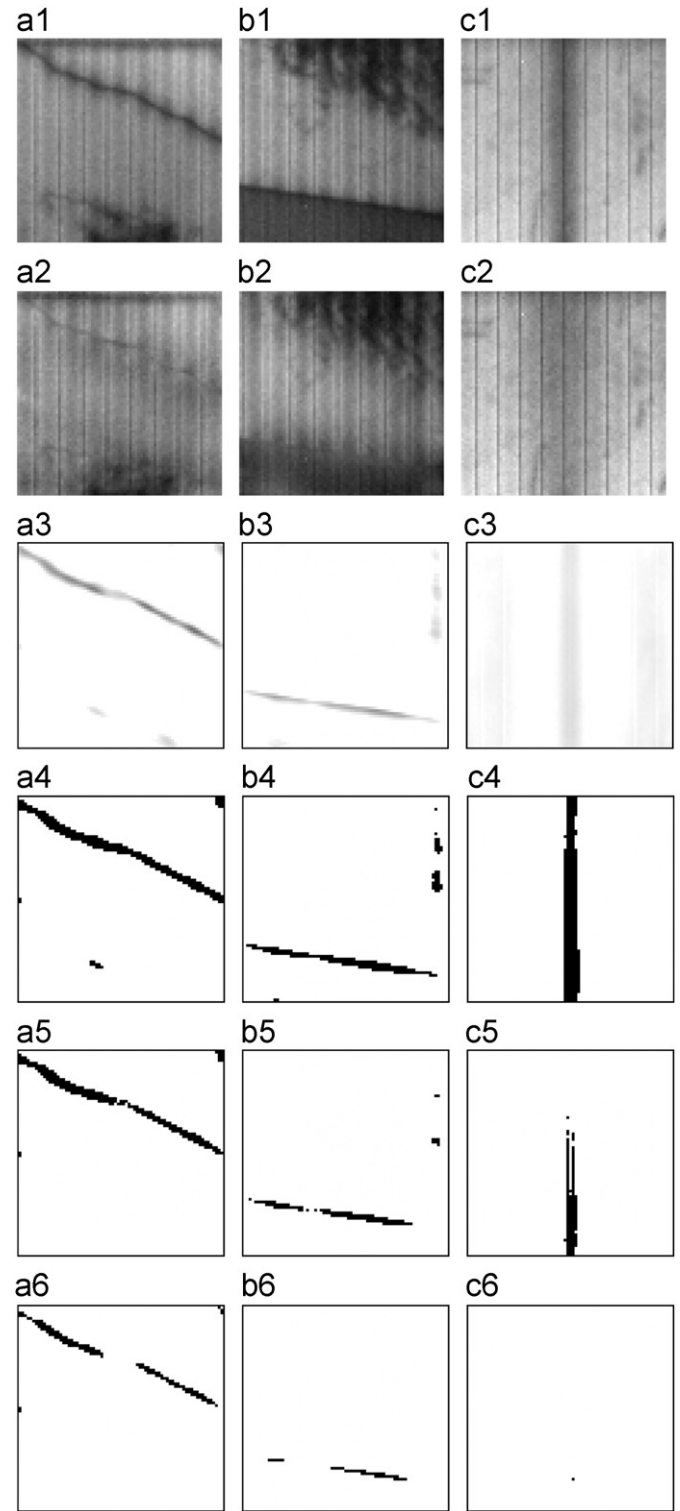


Fig. 13. Effect of changes in control constant $K_{\Delta f}$ for defective solar cells: (a1)–(c1) defective EL subimages with small crack, break and finger interruption, respectively; (a2)–(c2) respective reconstructed images; (a3)–(c3) respective difference images; (a4)–(c4) segmentation results with $K_{\Delta f} = 1$; (a5)–(c5) segmentation results with $K_{\Delta f} = 1.5$; (a6)–(c6) segmentation results with $K_{\Delta f} = 2$.

$K_{\Delta f} = 1, 1.5$ and 2 , respectively. The results in Fig. 12 show that no noise is present in the binary images of defect-free solar cells, even with a tight control constant of 1 . This absence of noise indicates

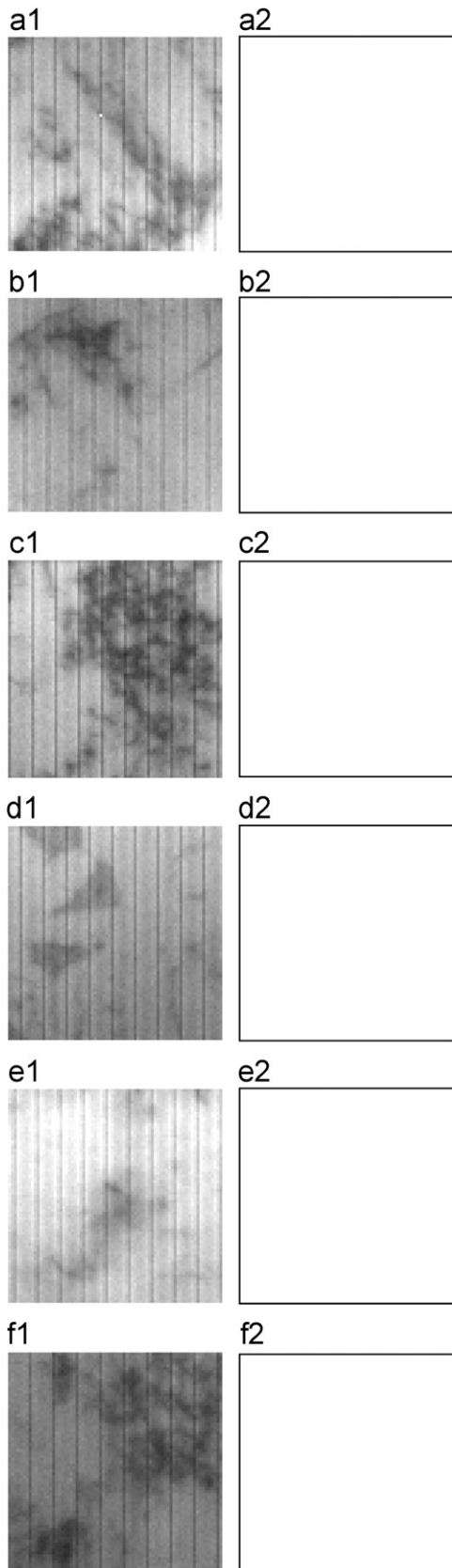


Fig. 14. Detection results on defect-free solar cells: (a1)–(f1) EL subimages; (a2)–(f2) respective segmentation results.

that the defect-free EL images are highly tolerant to the change of $K_{\Delta f}$ value in a wide range. A large control constant $K_{\Delta f} = 2$ causes mis-detection of the blurred finger interruption, as seen in Fig. 13(c6). The $K_{\Delta f}$ value of 1 gives more complete shapes of detected defects. Since a small $K_{\Delta f}$ value of 1 is tolerant to noise for defect-free EL images and gives better segmentation of defects, it is therefore used in the subsequent experiments for all test samples.

3.3. Performance evaluation

This subsection demonstrates the detection results of various multicrystalline solar cells in EL images. The parameter values are fixed with band-rejection width $\Delta w = 5$ and control constant $K_{\Delta f} = 1$ for all test samples in the experiment. Figs. 14(a1)–(f1) shows a set of six defect-free EL subimages of various solar cell surfaces, where random dark regions are present in the background. Fig. 14(e1) displays a very bright EL subimage, whereas Fig. 14(f1) gives a dark, dim EL subimage. The detection results of Figs. 14(a1)–(f1) with the same parameter setting are present in Figs. 14(a2)–(f2). The results show uniformly white images and indicate no defects in the original EL images. Figs. 15(a1)–(f1) present, respectively, two small cracks, two breaks and two finger interruptions in the EL subimages. All six defects appear with cloud-shaped backgrounds in the EL images. The detection results are displayed as binary images, and are shown in Figs. 15(a2)–(f2). The results indicate that the proposed self-reference method with the Fourier image reconstruction can well detect the small, local defects in EL images with inhomogeneous backgrounds.

In an additional experiment, we have also evaluated a total of 323 EL subimages of solar cells, of which 308 are defect-free samples and 15 are defective samples containing various defects of small cracks, breaks, and finger interruptions. Since the proposed defect detection method is based on EL imaging, all the 323 test samples were visually examined by human inspectors from the EL images, and were manually classified into defect-free and defective samples. The proposed method, with the same parameter settings of $\Delta w = 5$ and $K_{\Delta f} = 1$, identifies correctly the defects in all 15 defective samples, and declares no false alarms for all 308 defect-free samples. The proposed method yields consistent detection results as the human inspectors.

4. Conclusions

In this paper, we have proposed a self-reference scheme based on the Fourier image reconstruction to detect various defects in multicrystalline solar cells. Small cracks, breaks, and finger interruptions are severe defects found in solar cells. Some of the defects, such as interior small cracks, cannot be visually observed in the image with the conventional CCD imaging system. The electroluminescence imaging technique is thus used to highlight the defects in the sensed image. The target defects mostly present as line- or bar-shaped objects in the EL image. To identify defects in the inhomogeneous surface of an EL image, the Fourier image reconstruction process is applied to remove the possible defects in the EL image by setting the frequency components associated with the line- and bar-shaped defects to zero and then back-transforming to the spatial image. The difference image between the original EL image and its reconstructed image can then intensify the defect regions. A simple statistical control limit is finally used to segment defects from the background in the difference image.

Experimental results show that the proposed method can effectively detect various defects and performs stably for defect-free images with random dark regions in the background.

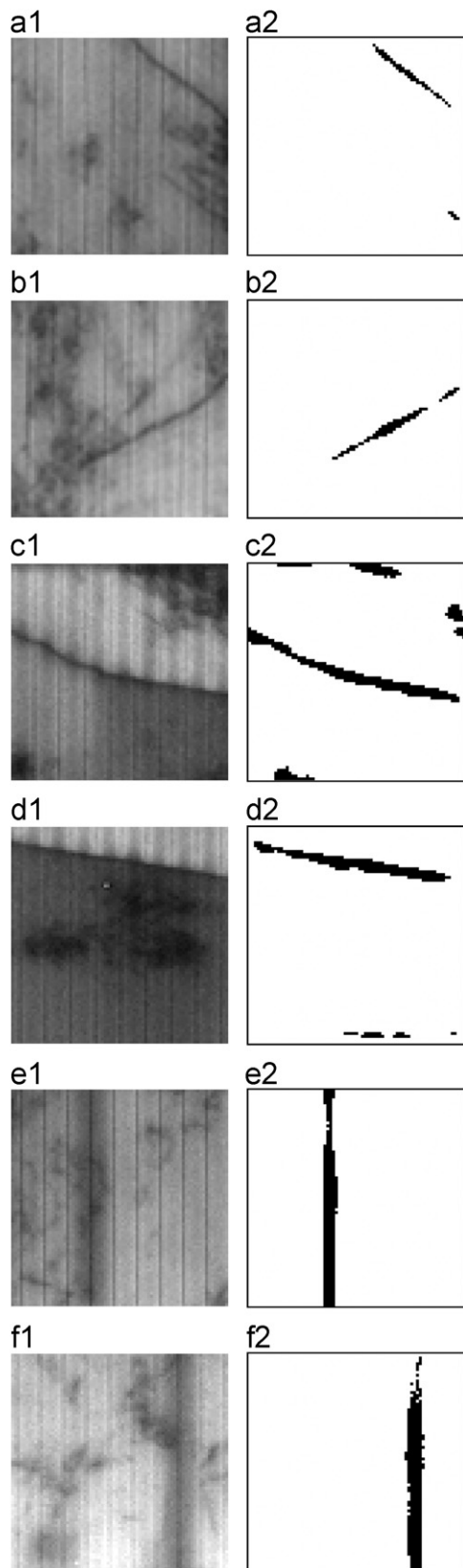


Fig. 15. Detection results on defective solar cells: (a1), (b1) EL subimages with small cracks; (c1), (d1) EL subimages with breaks; (e1), (f1) EL subimages with finger interruptions; (a2)–(f2) respective segmentation results.

Although the proposed method is based on the Fourier transform, it can be efficiently applied to a small subimage and achieves an average computation time of 0.29 s for a whole solar cell image of

size 550×550 pixels. It can be practically implemented for on-line, real-time defect inspection in solar cell manufacturing.

Experimental results also show that the two main parameters of the proposed method, band-rejection width $\Delta\omega$ and control constant $K_{\Delta\omega}$, can be tolerant in a moderate range. The fine-tuned parameter values of $\Delta\omega$ and $K_{\Delta\omega}$ for best detection results are generally related to the image size and resolution in question. It would be worthwhile to further investigate automatic selection of adaptive parameter values for changes of image size and image resolution.

References

- [1] T. Fuyuki, H. Kondo, T. Yamazaki, Y. Takahashi, Y. Uraoka, Photographic surveying of minority carrier diffusion length in polycrystalline silicon solar cells by electroluminescence, *Applied Physics Letters* 86 (2005) 262108.
- [2] T. Fuyuki, A. Kitiyanan, Photographic diagnosis of crystalline silicon solar cells utilizing electroluminescence, *Applied Physics A* 96 (2009) 189–196.
- [3] X. Xie, A review of recent advances in surface defect detection using texture analysis techniques, *Electron Letters Computer Vision and Image Analysis* 7 (2008) 1–22.
- [4] R.M. Haralick, K. Shanmugam, I. Dinstein, Texture features for image classification, *IEEE Transactions on Systems Man, and Cybernetics SMC-3* (1973) 610–621.
- [5] K.V. Ramana, B. Ramamoorthy, Statistical methods to compare the texture features of machined surfaces, *Pattern Recognition* 29 (1996) 1447–1459.
- [6] J. Iivarinen, K. Keikkinen, J. Rauhamaa, P. Vuorimaa, A. Visa, A defect detection scheme for web surface inspection, *International Journal of Pattern Recognition and Artificial Intelligence* 14 (2000) 735–755.
- [7] R. Pan, W. Gao, J. Jiu, H. Wang, Automatic recognition of woven fabric pattern based on image processing and BP neural network, *Journal of Textile Institute* 102 (2011) 19–30.
- [8] J. Li, Y. Lu, B. Pu, Y. Xie, J. Qin, W.-M. Pang, P.-A. Heng, An automated cotton contamination detection system based on co-occurrence matrix contrast information, in: *IEEE International Conference on Intelligent Computing and Intelligent Systems*, Shanghai, China, 2009, pp. 517–521.
- [9] S.S. Liu, M.E. Jernigan, Texture analysis and discrimination in additive noise, *Computer Vision, Graphics Image Process* 49 (1990) 52–67.
- [10] C.H. Chan, G.K.H. Pang, Fabric defect detection by Fourier analysis, *IEEE Transactions on Industry Applications* 36 (2000) 1267–1276.
- [11] A. Kumar, Computer-vision-based fabric defect detection: a survey, *IEEE Transactions on Industrial Electronics* 55 (2008) 348–363.
- [12] T. Ohshige, H. Tanaka, Y. Miyazaki, T. Kanda, H. Ichimura, N. Kosaka, T. Tomoda, Defect inspection system for patterned wafers based on the spatial-frequency filtering, in: *IEEE/CHMT Int. Electronic Manuf. Technol. Symp.*, San Francisco, CA, USA, 1991, pp. 192–196.
- [13] G. Paschos, Fast color texture recognition using chromaticity moments, *Pattern Recognition Letters* 21 (2000) 837–841.
- [14] K. Wiltzchi, A. Pinz, T. Lindeberg, Automatic assessment scheme for steel quality inspection, *Machine Vision and Applications* 12 (2000) 113–128.
- [15] A. Kumar, G. Pang, Defect detection in textured materials using Gabor filters, *IEEE Transactions on Industrial Applications* 38 (2002) 425–440.
- [16] A. Bodnarova, M. Bennamoun, S. Latham, Optimal gabor filters for textile flaw detection, *Pattern Recognition* 35 (2002) 2973–2991.
- [17] S.G. Mallat, A theory for multiresolution signal decomposition: the wavelet representation, *IEEE Transactions on Pattern Analysis and Machine Intelligence* 11 (1989) 674–693.
- [18] T. Chen, C.C.J. Kuo, Texture analysis and classification with tree-structured wavelet transform, *IEEE Transactions on Image Processing* 2 (1993) 429–441.
- [19] K. Maruo, T. Shibata, T. Yamaguchi, M. Ichikawa, T. Ohmi, Automatic defect pattern detection on LSI wafers using image processing techniques, *IEICE Transactions on Electronics E82-C* (1999) 1003–1012.
- [20] J. Scharcanski, Stochastic texture analysis for monitoring stochastic processes in industry, *Pattern Recognition Letters* 26 (2005) 1701–1709.
- [21] X. Yang, G. Pang, N. Yung, Robust fabric defect detection and classification using multiple adaptive wavelets, *IEEE Proceedings Vision, Image Processing* 152 (2005) 715–723.
- [22] Z. Fu, Y. Zhao, Y. Liu, Q. Cao, M. Chen, J. Zhang, J. Lee, Solar cell crack inspection by image processing, in: *International Conference on the Business of Electronic Product Reliability and Liability*, Shanghai, China, 2004, pp. 77–80.
- [23] M.A. Ordaz, G.B. Lush, Machine vision for solar cell characterization, in: *Proc. of SPIE*, San Jose, CA, USA, 2000, pp. 238–248.
- [24] M. Pilla, F. Galmiche, X. Maldague, Thermographic inspection of cracked solar cells, in: *Proc. of SPIE*, Seattle, WA, USA, 2002, pp. 699–703.
- [25] M. Demant, M. Glatthaar, J. Haunschild, S. Rein, Analysis of luminescence images applying pattern recognition techniques, in: *Proceedings of the 5th World Conference on Photovoltaic Energy Conversion*, Valencia, Spain, pp. 1078–1082, 2010.
- [26] J. Haunschild, M. Glatthaar, M. Demant, J. Nievendick, Quality control of as-cut multicrystalline silicon wafers using photoluminescence imaging for solar cell production, *Solar Energy Materials and Solar Cells* 94 (2010) 2007–2012.

- [27] W. Warta, Defect and impurity diagnostics and process monitoring, *Solar Energy Materials and Solar Cells* 72 (2002) 389–401.
- [28] D.M. Tsai, C.C. Chang, S.-M. Chao, Micro-crack inspection in heterogeneously textured solar wafers using anisotropic diffusion, *Image and Vision Computing* 28 (2010) 491–501.
- [29] D.M. Tsai, J.Y. Luo, Mean shift-based defect detection in multicrystalline solar wafer surfaces, *IEEE Transactions on Industrial Informatics* 7 (2011) 125–135.
- [30] Y.C. Chiou, F.Z. Liu, Micro crack detection of multi-crystalline silicon solar wafer using machine vision techniques, *Sensor Review* 31 (2011) 154–165.
- [31] W.C. Li, D.M. Tsai, Automatic saw-mark detection in multicrystalline solar wafer images, *Solar Energy Materials and Solar Cells* 95 (2011) 2206–2220.
- [32] B.H. Khalaj, H.K. Aghajan, T. Kailath, Patterned wafer inspection by high resolution spectral estimation techniques, *Machine Vision and Applications* 7 (1994) 178–185.
- [33] S.U. Guan, P. Xie, H. Li, A golden-block-based self-refining scheme for repetitive patterned wafer inspections, *Machine Vision and Applications* 13 (2003) 314–321.
- [34] D.M. Tsai, C.Y. Hsieh, Automated surface inspection for directional textures, *Image and Vision Computing* 18 (1999) 49–62.
- [35] D.M. Tsai, T.Y. Huang, Automated surface inspection for statistical textures, *Image and Vision Computing* 21 (2003) 307–323.